

Highly Selective and Sensitive Ratiometric Detection of Sn²⁺ Ions Using NIR-Excited Rhodamine-B-Linked Upconversion Nanophosphors

Jitender Kumar and Indrajit Roy*

Cite This: *ACS Omega* 2022, 7, 29840–29849

Read Online

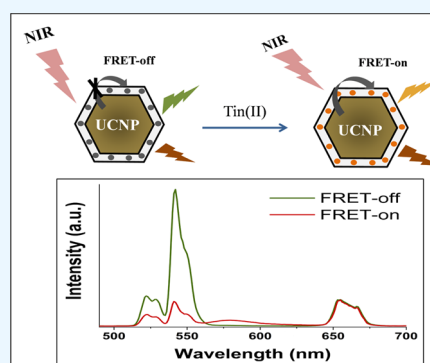
ACCESS |

Metrics & More

Article Recommendations

Supporting Information

ABSTRACT: Detection of Sn²⁺ ions in environmental and biological samples is essential owing to the toxicological risk posed by excess use tin worldwide. Herein, we have designed a nanoprobe involving upconversion nanophosphors linked with a rhodamine-based fluorophore, which is selectively sensitive to the presence of Sn²⁺ ions. Upon excitation with near-infrared (NIR) light, the green emission of the nanophosphor is reabsorbed by the fluorophore with an efficiency that varies directly with the concentration of the Sn²⁺ ions. We have explored this NIR-excited fluorescence resonance energy transfer (FRET) process for the quantitative and ratiometric detection of Sn²⁺ ions in an aqueous phase. We have observed an excellent linear correlation between the ratiometric emission signal variation and the Sn²⁺ ion concentration in the lower micromolar range. The detection limit of Sn²⁺ ions observed using our FRET-based nanoprobe is about 10 times lower than that observed using other colorimetric or fluorescence-based techniques. Due to the minimal autofluorescence and great penetration depth of NIR light, this method is ideally suited for the selective and ultrasensitive detection of Sn²⁺ ions in complex biological or environmental samples.



INTRODUCTION

Tin is one of the most widely utilized heavy metals in industry. It is used in both organic and inorganic forms, with applications as diverse as antifouling paints, agrochemicals, poly(vinyl chloride) (PVC) stabilizers, catalysts, biocides, etc. Owing to such widespread use, over the last few decades, an excessive amount of inorganic and organic tin has been released into the environment, as a result of which it is found in large amounts in the air, water, and soil.^{1–4} When these metal ions reach the human body through the food chain, they have a major detrimental influence on health and induce a variety of ailments.^{5–8} Tin doses of more than 130 mg/kg have been seen to accumulate in the kidneys, bones, and spleen.^{9–11} Tin(II) ions can induce diarrhea and DNA damage in the respiratory, reproductive, nervous, and digestive systems. Nausea, vomiting, and upper respiratory tract discomfort are all symptoms of moderate tin poisoning.^{12–16} Acute tin poisoning can result in permanent renal tubule damage and various neurological alterations leading to disorientation, confusion, and memory loss, as well as severe epileptic seizures.^{17–19} Therefore, methods of monitoring tin ion concentrations in environmental and biological samples are essential.

A number of analytical methods have been used for the detection/screening of Sn²⁺ ions, which include direct ion-concentration measurements such as atomic absorption spectroscopy and microwave-induced atomic emission spec-

troscopy, or indirect, probe-based techniques such as electrochemical, colorimetric, and fluorometric assays. The direct methods, although provide good selectivity and sensitivity of detection, are expensive and tedious, which makes them unsuitable for real-time and *in situ* analysis.^{20–23} Electrochemical methods, which rely on differences in the redox potential of ions, have poor selectivity and reproducibility. Certain colorimetry and fluorometry-based analytical chemosensors, using organic dyes and nanoparticles, have been developed for the selective detection of tin ions.^{24–26} These sensors have good selectivity but show poor sensitivity and reproducibility, thus providing limited detection efficiency. Also, these sensors are usually excited by high-energy light within the UV–vis region, making them less likely to be utilized in the biological system due to the short penetration depth of UV–vis light. Autofluorescence and a poor signal-to-noise ratio are two apparent issues that degrade sensing performance and photo-oxidize sensing probes.^{27–29} As a result, the development of advanced sensing probes activated by NIR light is urgently required.

Received: April 29, 2022

Accepted: August 4, 2022

Published: August 17, 2022



The sensitivity and depth profiling of these optical sensors can be improved with the use of near-infrared (NIR) light as the primary excitation source. The NIR light is better suited as an excitation source because it penetrates deeper into the tissue and causes less harm to biological material than UV light.^{30–35} Recently, lanthanide-doped upconverting nanophosphors (UCNPs) have attracted significant interest in biological, analytical, and optoelectronic applications because of their ability to convert NIR excitation light into shorter wavelength light. In addition, they have several other appealing optical and chemical features, including high Stokes shift, low toxicity, weak autofluorescence backgrounds, and resistance to photobleaching.^{36–39} UCNPs constitute a dilute guest–host system, in which lanthanide ions are doped as a guest in an appropriate dielectric host lattice.^{40–43} UCNPs absorb two or more photons sequentially, resulting in the emission of a single high-energy (low-wavelength) photon.^{44–47} Several studies have shown that these characteristics make UCNPs an excellent choice for use as an energy donor in nanoprobe based on fluorescence resonance energy transfer (FRET).^{48–50} So far, numerous sensors have been designed based on FRET to detect DNA, metal ions, and small molecules, in which UCNPs transmit energy to other chromophores, resulting in measurable changes in emission intensity/pattern.

Herein, we have designed an UCNP-based chemosensor involving an Sn^{2+} -sensitive fluorescent probe (rhodamine-B derivative, or RBD) covalently linked to poly(acrylic acid) (PAA)-coated UCNPs (UCNP@PAA) and investigated its application in the ultrasensitive detection of Sn^{2+} ions. Both UV–vis absorbance and fluorescence emission properties of RBD are highly sensitive toward Sn^{2+} concentration in the solution. The UCNPs act as an energy donor that converts incident NIR light (of wavelength 980 nm) into visible light for exciting RBD (energy acceptor). We have probed in detail the FRET process between the UCNPs (characterized by the attenuation in their green emission peaks) and attached RBD molecules (characterized by concurrent enhancement in their red emission peak) as a function of the concentration of Sn^{2+} ions in the solution. Such FRET process allows ratiometric detection of the analyte, which enhances the reproducibility and sensitivity of analysis when compared to that obtained using traditional, single-mode analytical methods. Therefore, this work combines the advantages of the high selectivity of tin-ion detection using an organic probe (RBD) with the high sensitivity and reproducibility offered by FRET-based ratiometric detection involving UCNPs as an energy donor and RBD as an energy acceptor and the high tissue penetration of incident NIR light for potentially background-free detection in biological specimens. Based on the observed data, we have carried out a ratiometric analysis of the intensities of these emission bands and plotted the ratios against the concentration of Sn^{2+} ions. Based on the data obtained, we compared the detection limit of Sn^{2+} ion sensing obtained with our technique with those of some other published reports.

EXPERIMENTAL SECTION

Materials. All of the chemicals were utilized without additional purification. $\text{Y}(\text{NO}_3)_3 \cdot 6\text{H}_2\text{O}$ (99.99%), $\text{Yb}(\text{NO}_3)_3 \cdot 6\text{H}_2\text{O}$ (99.99%), $\text{Er}(\text{NO}_3)_3 \cdot 6\text{H}_2\text{O}$ (99.99%), diethylene glycol, poly(acrylic acid) (PAA), and ethylenediamine (reagent, 99%) were purchased from Sigma-Aldrich. Oleic acid (90%, technical grade), 1-octadecene (90%, technical grade), and hydrochloric acid (HCl, analytical reagent 35–38%) were purchased from

Alfa Aesar. Rhodamine-B (RhB, 95%) and hydrazine hydrate 80 wt% solution in H_2O were purchased from Loba Chemie Pvt. Ltd. Ammonium fluoride (NH_4F , 99%), sodium hydroxide (NaOH , 97%), cyclohexane (C_6H_{12} , 99%), ethanol ($\text{C}_2\text{H}_5\text{OH}$, analytical reagent 99%), and methanol (CH_3OH , analytical reagent 99%) were purchased from Spectrochem Pvt. Ltd. Double distilled water was utilized to prepare all of the aqueous solutions. Aqueous solutions of Sn^{2+} , Hg^{2+} , Co^{2+} , Mg^{2+} , Ni^{2+} , Ca^{2+} , Zn^{2+} , Co^{2+} , Cd^{2+} , Na^+ , K^+ , and Cs^+ were made from the corresponding halide salts.

Synthesis of Upconverting Nanophosphors ($\text{NaYF}_4:\text{Yb}^{3+}/\text{Er}^{3+}$). Uniform UCNPs ($\text{NaYF}_4:\text{Yb}^{3+}/\text{Er}^{3+}$) capped with oleic acid (OA) were prepared via solvothermal synthesis.⁵¹ In a typical synthesis, 0.795 mmol of $\text{Y}(\text{NO}_3)_3 \cdot 6\text{H}_2\text{O}$, 0.20 mmol of $\text{Yb}(\text{NO}_3)_3 \cdot 6\text{H}_2\text{O}$, and 0.005 mmol of $\text{Er}(\text{NO}_3)_3 \cdot 6\text{H}_2\text{O}$ were taken in a 100 mL round-bottom flask. Then, 15 mL of octadecene and 5 mL of OA were added. A homogeneous solution was formed upon heating to 160 °C for 30 min, after which the solution was cooled to room temperature. Then, 10 mL of the methanol solution containing 0.148 g of NH_4F and 0.1 g of NaOH was added to the flask and heated to 60–80 °C to remove methanol from the reaction. The solution was then degassed at 100 °C for 10 min and heated under N_2 protection to 300 °C. The solution was naturally cooled to room temperature after being held at 300 °C for 1.5 h. The product $\text{NaYF}_4:\text{Yb}^{3+}/\text{Er}^{3+}$ nanophosphors were precipitated with ethanol from the solution and washed and centrifuged using ethanol and cyclohexane to collect the nanoparticles.

Synthesis of PAA-Coated Upconverting Nanophosphors. The ligand-exchange approach was used to coat the surface of nanophosphors with poly(acrylic acid) (PAA).⁵² In a three-necked flask, 0.5 g of PAA was added to 10 mL of diethylene glycol (DEG), and the mixture was vigorously stirred at 110 °C to obtain a clear solution. One hundred mg of UCNPs was dispersed in 5 mL of cyclohexane and slowly added to the reaction mixture. Then, the above reaction mixture was refluxed at 150 °C for 150 min in the presence of nitrogen. After refluxing, the resulting mixture was heated to 240 °C for 30 min to remove the cyclohexane. After cooling the solution to room temperature, ethanol was added to form a precipitate. The PAA-coated nanophosphors were collected by centrifugation and washed three times with ethanol/water (1:1 v/v).

Synthesis of Rhodamine-B Derivative (RBD). The derivative of rhodamine-B was synthesized by a simple reaction. First, 0.5 g of rhodamine-B was dissolved in 15 mL of ethanol. Then, ethylenediamine (2 mL, excess) was added dropwise to the solution with vigorous stirring, and the mixture was refluxed for 24 h at 90 °C. The resulting solution was pale orange in color. The mixture was then allowed to cool to room temperature before extracting the solvent under decreased pressure using a rotatory evaporator. Twenty-five and 15 mL of 0.1 M of HCl and 1 M of NaOH solutions, respectively, were prepared. The as-prepared HCl solution was added dropwise to the mixture until gas production was stopped to obtain a red solution. Then, the NaOH solution was progressively added and agitated until the pH of the solution reached around 10. To eliminate the remaining impurities, the precipitate was centrifuged and rinsed five times with distilled water. The resulting material was dried under a vacuum at 60 °C for 8 h to obtain a cream-colored solid with excellent yield.

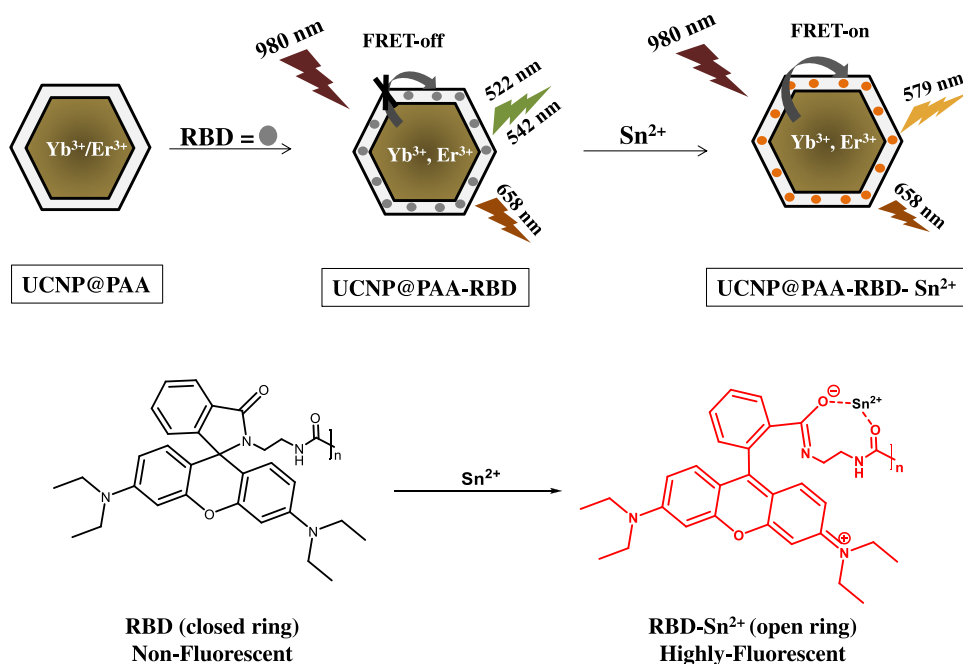


Figure 1. Schematic illustration of the synthetic procedure of UCNP@PAA-RBD and the proposed FRET-based sensing mechanism of UCNP@PAA-RBD with Sn²⁺ ions.

Synthesis of UCNP@PAA-RBD. In 10 mL of double distilled water, 50 mg of PAA-coated UCNPs were taken and sonicated for 5 min. Another solution of 50 mg of RBD was prepared in 1 mL of water, followed by the addition of 100 μ L of ethanol. Then, the RBD solution was added to the UCNP dispersion and stirred for 24 h at room temperature. In the reaction mixture, the free carboxylic groups of PAA-coated UCNPs reacted with ethanol to form the corresponding polyacrylate ester. Then, this ester reacted with the free amine groups of RBD to form an amide linkage between the UCNP and RBD. The RBD-modified UCNPs (UCNP@PAA-RBD) were collected after centrifugation and washed three times with ethanol.

Detection of Tin Ions. In deionized water, stock solutions of Sn²⁺ and other metal ions (0.1 mM) were prepared. A stock solution of RBD (3 mg/mL) and UCNP@PAA-RBD (3 mg/mL) nanophosphors were prepared in distilled water. The selectivity of metal ions was determined as follows. First, we took 100 μ L of the RBD stock solution in 3 mL of water and added suitable volumes of metal ions, including tin ions, to it. Then, UV-vis and fluorescence spectra of the resulting solutions were recorded. For the detection, the same amount of RBD stock solution in 3 mL of water was taken. Then, different amounts of Sn²⁺ ions (in μ M) were added using a micropipette, followed by the recording of UV-vis and fluorescence spectra. For the FRET-based detection, 100 μ L of the stock solution of UCNP@PAA-RBD was added to 3 mL of water, and the upconverting photoluminescence spectra were recorded with different concentrations of Sn²⁺ ions (in ppm) under the NIR light (980 nm) excitation.

Characterization. The nanophosphors were subjected to morphological characterization by field emission scanning electron microscopy (FESEM) using scanning transmission electron microscopy (STEM), MERLIN Zeiss-Germany. For that, the suspension of nanophosphors was deposited on a copper TEM grid with a carbon film (TED Pella). To confirm the exact shape and size of the nanoparticles, transmission

electron microscopy (TEM) was carried out using a TECNAI G²-30 U TWIN (FEI, Eindhoven, Netherlands) instrument operated with an accelerated voltage of 300 kV. The average hydrodynamic diameter of the nanophosphors was measured by dynamic light scattering (DLS), using a NANO-ZS series Malvern Zetasizer instrument. Powder X-ray diffraction measurement was done to analyze the phase composition and crystalline nature of nanophosphors using a Bruker D8 Discover X-ray spectrometer, which utilizes Cu K α radiation ($\lambda = 1.54060 \text{ \AA}$) over the 2θ range at the rate of 2.58/min. FT-IR spectra were taken from the range of 4000 to 400 cm⁻¹, where dried and powdered nanophosphors were mixed with KBr and the mixture was passed into a pellet for analysis using a PerkinElmer RX1 spectrometer. The absorbance and fluorescence spectra were observed using a Shimadzu UV-1601 spectrophotometer (Shimadzu, Kyoto, Japan) and a Cary Eclipse fluorescence spectrometer (Varian, Palo Alto, CA), respectively. An upconversion fluorescence spectrometer (Quanta Master, Model QM-8450-11), attached with an external 980 nm tunable diode laser, was used to acquire the upconversion luminescence emission spectra.

RESULTS AND DISCUSSION

We first synthesized hexagonal (β -phase) UCNPs (NaYF₄:Yb³⁺/Er³⁺) via the solvothermal method, with NaYF₄ serving as the host matrix and dopant ions Yb³⁺ and Er³⁺ as sensitizer and activator, respectively. These UCNPs were hydrophobic and well dispersed in cyclohexane. PAA coating was done on the surface of UCNPs to make them hydrophilic using the ligand-exchange approach, which not only results in their optimal aqueous dispersion but also provides free functional groups for further conjugation reactions. The fabrication of the Sn²⁺-sensitive FRET-based probe is enabled by the covalent linkage between PAA-modified UCNPs and ethylenediamine-tagged derivative of rhodamine-B (RBD). This linkage during simple mixing results in the strong binding of the acceptor (RBD) to the donor (UCNP) surface. The

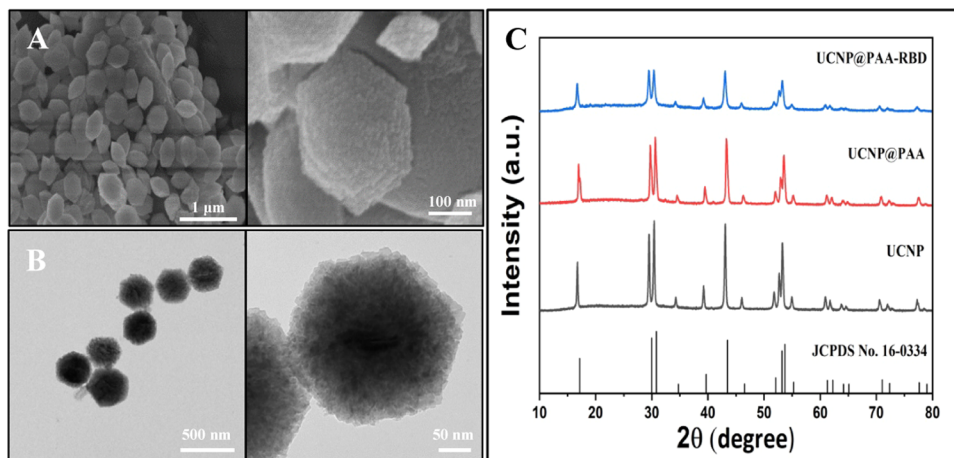


Figure 2. Low- and high-resolution (A) FESEM and (B) TEM images of UCNPs. (C) XRD patterns of the UCNP, UCNP@PAA, and UCNP@PAA-RBD, along with the standard (JCPDS No. 16-0334).

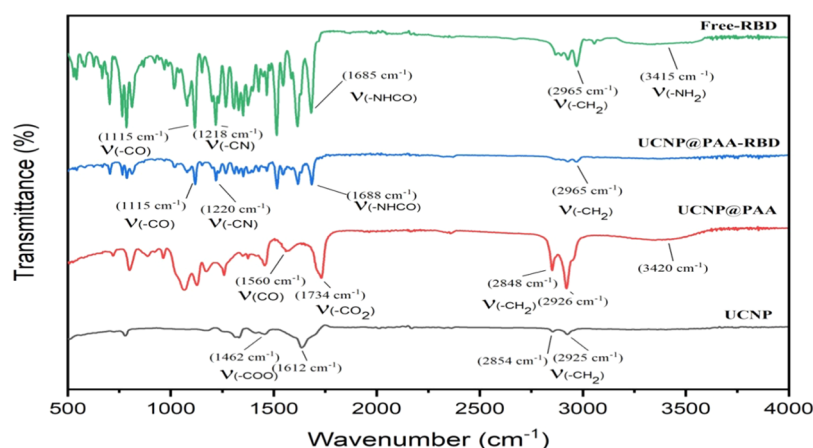


Figure 3. FT-IR spectra of UCNP, UCNP@PAA, UCNP@PAA-RBD, and free RBD.

RBD molecule, whether free or bound to the UCNPs, undergoes a structural transition from a closed-ring (non-fluorescent) to an open-ring (fluorescent) configuration as a result of the coordination with Sn²⁺ ions. As the NIR-excited green emission peak of the UCNP overlaps with the absorption spectrum of the open-ring (Sn²⁺-coordinated) form of RBD, it is evident that with the increasing Sn²⁺ concentration, FRET from UCNP (donor) to open-ring RBD (acceptor) is enhanced, leading to the simultaneous decrease and increase in the emission peaks of UCNP (green emission) and RBD, respectively. This facilitates the ratiometric and quantitative detection of Sn²⁺ ions *via* the FRET process under NIR excitation, as shown schematically in Figure 1.

The structural and morphological characterization of nanophosphors was done by utilizing FESEM and TEM. The low- and high-resolution FESEM images showed that UCNPs were synthesized with uniform sizes and had a hexagonal morphology (Figure 2A). From the low- and high-resolution TEM micrographs (Figure 2B), it is evident that UCNPs are hexagonal, with size in the range of 150–250 nm, thus validating the FESEM data. The average size and polydispersity index (PDI) of the UCNPs, as evident from DLS measurements, were measured to be 186.5 nm and 0.184, respectively (Figure S1). The X-ray diffraction (XRD) patterns of UCNP, UCNP@PAA, and UCNP@PAA-RBD are shown in Figure 2C. The XRD pattern of all UCNP samples was in good

agreement with the standard database (JCPDS 16-0334),⁵³ validating the pure hexagonal phase of the UCNPs. No additional peaks were found, indicating the purity of the prepared product. The sharp peaks seen in the XRD pattern indicated the crystalline nature of the synthesized material. The sharpness of peaks of UCNP@PAA and UCNP@PAA-RBD was reduced because of the coating of PAA on the nanophosphors. The existence of Na, Y, F, Yb, and Er in the prepared samples was confirmed by the energy-dispersive X-ray (EDX) spectrum (Figure S2).

Figure 3 shows the Fourier transform infrared (FT-IR) spectra of UCNP, UCNP@PAA, and UCNP@PAA-RBD recorded in the 500–4000 cm⁻¹ range. The FT-IR spectrum of the synthesized UCNPs shows four notable peaks at 1462, 1612, 2854, and 2925 cm⁻¹. The methylene (–CH₂–) asymmetric and symmetric stretching vibrations of OA in the long alkyl chain were attributed to the bands at 2925 and 2854 cm⁻¹. Moreover, asymmetric and symmetric stretching vibrations of the –COO– on the surface of the UCNPs resulted in two bands centered at 1612 and 1462 cm⁻¹, respectively. After PAA coating on the surface of nanophosphors, the asymmetric stretching vibrations of the –CO and –CO₂ groups of the PAA ligand at 1560 and 1734 cm⁻¹, respectively, were observed in the spectrum. The symmetric stretching vibrations of CH₂ caused another peak in the higher-wavenumber region, *i.e.*, 2926 cm⁻¹ (νCH₂). In addition, the

stretching vibration of the hydroxyl (–OH) group caused a wide singlet at 3443 cm^{-1} . The results showed that PAA successfully converted the hydrophobic surface of nanoparticles to hydrophilic. Also, three new peaks were observed at 1688 , 1220 , and 1115 cm^{-1} , which corresponded to the stretching frequencies of –NHCO, –C–N, and –CO groups. The peak of the –OH group in UCNP@PAA disappeared, indicating its utility in forming a covalent linkage with RBD. This was further confirmed by the absence of the –NH₂ peak (of free RBD) in the UCNP@PAA-RBD conjugate.

The synthesized UCNPs emitted characteristic emission bands at 407 nm (blue), 522 nm , 542 nm (both green), and 655 nm (red), under the NIR laser excitation of 980 nm

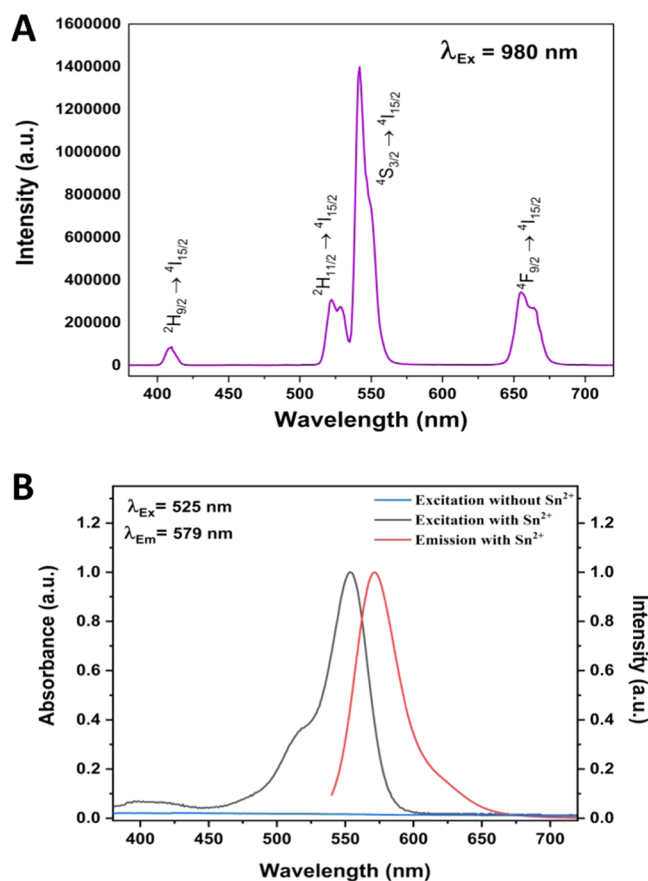


Figure 4. (A) Photoluminescence spectrum of UCNPs under NIR (980 nm) laser excitation. (B) Excitation and emission spectra of RBD, with and without added Sn^{2+} ions.

(Figure 4A). These bands corresponded to Er^{3+} ion transitions ${}^2\text{H}_{9/2} \rightarrow {}^4\text{I}_{15/2}$, ${}^2\text{H}_{11/2} \rightarrow {}^4\text{I}_{15/2}$, ${}^4\text{S}_{3/2} \rightarrow {}^4\text{I}_{15/2}$, and ${}^4\text{F}_{9/2} \rightarrow {}^4\text{I}_{15/2}$, as already reported in several publications.^{54–56} The structural and photoluminescence characteristics of RBD were also studied. The ${}^1\text{H}$ NMR and ${}^{13}\text{C}$ NMR spectra (Figure S3) of RBD showed that the compound was properly synthesized from rhodamine-B. The excitation and emission spectra of RBD in the presence of Sn^{2+} ions are shown in Figure 4B. It is evident from the graph that pure RBD (without added Sn^{2+}) displayed no apparent absorption/excitation. However, a broader, distinctive excitation band ranging from 495 to 590 nm ($\lambda_{\text{Em}} = 579\text{ nm}$), with a peak at 554 nm , was seen after the addition of Sn^{2+} ions, which overlapped well with the two green upconverting emission bands of UCNPs (at 522 and 542

nm). This data clearly shows the overlap between the green emission bands of the UCNPs and the absorption/excitation band of the open-ring RBD, indicating the feasibility of energy transfer from UCNPs to the open-ring RBD. Finally, the emission band of the open-ring RBD is observed with a maximum at around 579 nm ($\lambda_{\text{Ex}} = 525\text{ nm}$).

Figure 5A shows the UV–vis absorption spectra of free RBD treated with various metal ions, including Sn^{2+} ion. A noticeable enhancement in the absorption spectra of RBD (centered at 554 nm) is found only upon treatment with Sn^{2+} ion. This observation is visibly evidenced by the change in the probe's color from colorless to magenta upon treatment with Sn^{2+} ions only (Figure 5B). This observation confirms the RBD's preferential affinity for Sn^{2+} ions over other metal ions. The Sn^{2+} ions can aid in the hydrolysis of RBD's α -amino acid ester ring, resulting in the formation of Sn - α -amino acid chelate due to the ring opening of RBD, as schematically illustrated earlier in Figure 1.

The UV–vis titration spectra of the RBD solution ($100\ \mu\text{L}$ of stock in 3 mL of water) after the addition of increasing amounts of Sn^{2+} ions (in the range of 0 – $50\ \mu\text{M}$) are shown in Figure 6A. The intensity of the absorption band centered at 554 nm grew noticeably with the linear increase in Sn^{2+} concentration. A calibration curve of the relative absorbance intensity of RBD as a function of added Sn^{2+} ion concentration is depicted in Figure 6B. It can be seen that the relative intensity increased linearly with the concentration, and showed an R^2 value of 0.9979 . The detection limit of RBD toward Sn^{2+} , which was calculated as thrice the deviation of the blank signal (3σ),⁵⁷ was found to be $0.15\ \mu\text{M}$.

The fluorescence spectrum of RBD toward various metal ions is shown in Figure S4A. Similar to the UV–vis spectral data, significant enhancement in the fluorescence intensity (at 579 nm) was observed after treatment of RBD with Sn^{2+} ions only, thus validating the preferential affinity of the dye for Sn^{2+} ions over other metal ions. In the fluorescence titration spectra (Figure 7A) of the RBD solution ($100\ \mu\text{L}$ of stock in 3 mL of water), a considerable increase in fluorescence intensity at 579 nm was recorded upon treatment with different concentrations of Sn^{2+} ions. The fluorescence intensities (at 579 nm) of RBD as a function of Sn^{2+} ion concentrations are shown in Figure 7A (inset). This intensity was found to be linearly dependent on the concentration of Sn^{2+} ions. The calibration curve with different concentrations of Sn^{2+} displayed a colinear relationship ($F/F_0 = 0.0212C_{\text{Sn}^{2+}} - 0.0152$, $R^2 = 0.9935$), as shown in Figure 7B. The detection limit (3σ) by utilizing fluorescence techniques was calculated to be $0.29\ \mu\text{M}$, indicating that we could detect ecologically relevant quantities of Sn^{2+} utilizing this approach. The time-dependent response of RBD toward Sn^{2+} ions was also examined by fluorescence spectroscopy. The response of RBD ($100\ \mu\text{L}$ of stock in 3 mL of water) to Sn^{2+} was quick, as shown in Figure S4B, and the peak signal was reached in approximately 40 s . This analysis demonstrated that the nanoprobe responded very fast to Sn^{2+} ions and might be conveniently used to monitor and evaluate Sn^{2+} levels.

Furthermore, we repeated the RBD-mediated Sn^{2+} detection experiment using UV–vis absorption and fluorescence measurements in a buffer with $\text{pH} = 7$. The data for absorption and fluorescence measurements are provided in Figures S5A,B and S6A,B, respectively. It is evident that the data obtained by carrying out the optical measurements in water are very similar to that obtained in the buffer solution of $\text{pH} 7$.

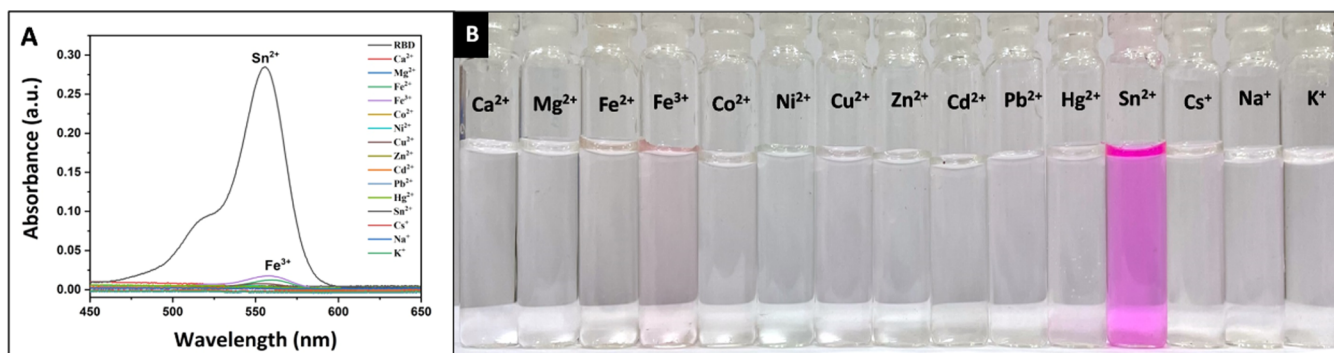


Figure 5. (A) UV-vis absorption spectra of RBD upon the addition of various metal ions (Ca^{2+} , Mg^{2+} , Fe^{2+} , Fe^{3+} , Co^{2+} , Ni^{2+} , Cu^{2+} , Zn^{2+} , Cd^{2+} , Pb^{2+} , Hg^{2+} , Sn^{2+} , Cs^{+} , Na^{+} , K^{+}) in distilled water. (B) Visible appearance of the solutions upon the addition of various metal ions, including Sn^{2+} .

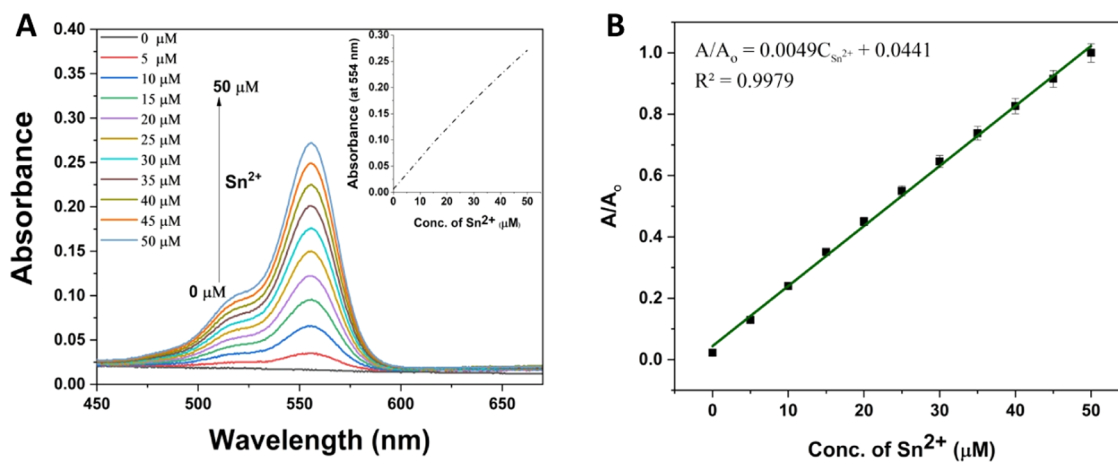


Figure 6. (A) Absorption changes of RBD with increasing amounts of Sn^{2+} ions. Inset: absorbance of RBD at 554 nm as a function of Sn^{2+} concentration. (B) Calibration plot for the relative absorption intensity at 554 nm of RBD as a function of Sn^{2+} concentration.

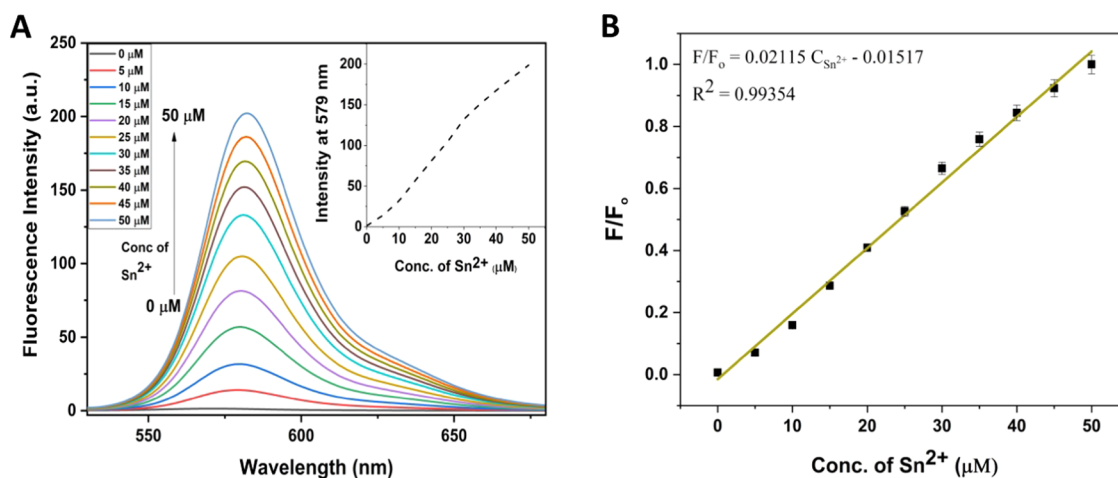


Figure 7. (A) Change in the fluorescence intensity of RBD with the increasing concentration of Sn^{2+} ions ($\lambda_{\text{Ex}} = 525 \text{ nm}$). Inset: fluorescence intensity at 579 nm as a function of Sn^{2+} ion concentration. (B) Relative fluorescence intensity at 579 nm of RBD as a function of Sn^{2+} ion concentrations.

We next investigated whether the detection sensitivity of Sn^{2+} ions can still be improved with the help of UCNP that allows FRET-based ratiometric analysis under excitation of deep-tissue-penetrating NIR light. First, the upconverting emission spectra of UCNP@PAA-RBD were analyzed using various concentrations of Sn^{2+} ions under NIR laser (980 nm) excitation. As mentioned previously, the green emission peak of UCNP and the absorption peak of the RBD- Sn^{2+}

combination overlaps, leading to fluorescence resonance energy transfer (FRET) from the UCNP to the RBD- Sn^{2+} complex under NIR excitation. As illustrated in Figure 8A, UCNP@PAA-RBD displays both green emission peaks and red emission peaks in the absence of Sn^{2+} ions. Next, when the Sn^{2+} ions are added to UCNP@PAA-RBD in increasing concentrations, the intensity of green emission peaks (at 522 and 542 nm) steadily decreases, while an additional, broader

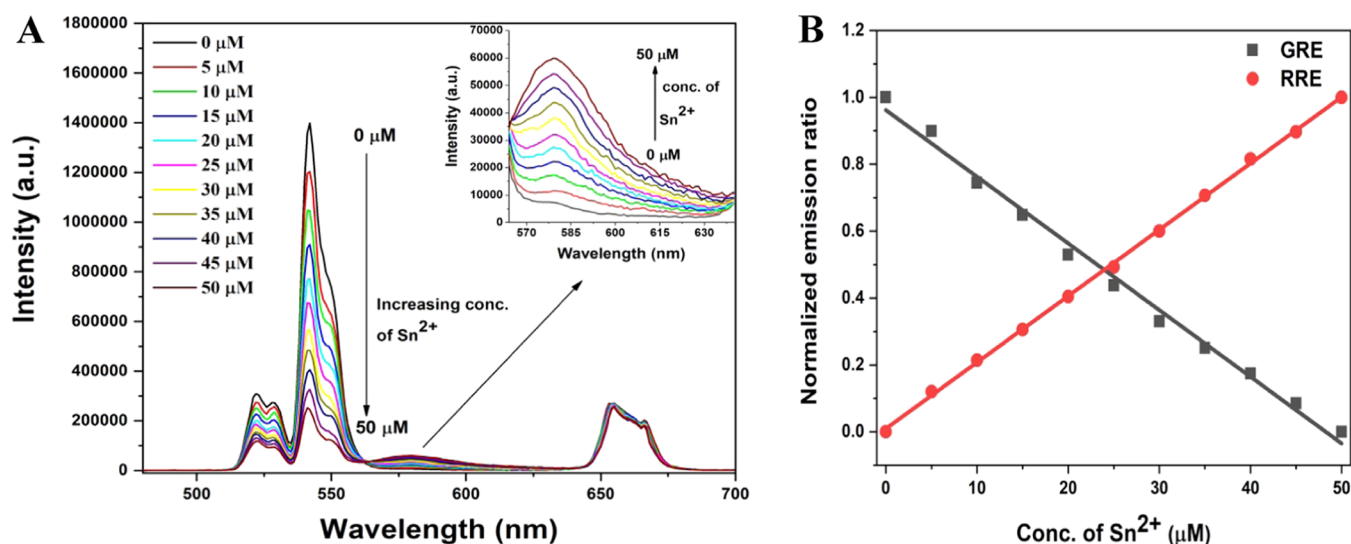


Figure 8. (A) Emission spectra of UCNP@PAA-RBD in the presence of the increasing concentration of Sn^{2+} ions upon 980 nm excitation. Inset: emission at 579 nm as a result of FRET upon the addition of Sn^{2+} ions. (B) Variation in normalized GRE and RRE at different concentrations of Sn^{2+} ions.

emission appears with a peak at 579 nm, which can be attributed to the attached RBD– Sn^{2+} complex. The energy transfer from the UCNPs to the RBD– Sn^{2+} complex is confirmed by a continuous drop in peaks of green emission and the appearance of a wide band at around 579 nm with the increasing concentration of Sn^{2+} ions, whereas the red emission of UCNPs at 655 nm remains almost consistent. The red emission intensity (at 655 nm) of UCNPs can be utilized as an internal reference since RBD does not absorb at this wavelength.

At different concentrations of Sn^{2+} ions, the green-to-red emission (GRE) ratios (I_{542}/I_{655}), as well as the RBD-to-red emission (RRE) ratio (I_{579}/I_{655}), are shown in Figure S7. Figure 8B shows the variation in both normalized GRE and RRE ratios at various concentrations of Sn^{2+} ions. The UCNP emission/RBD absorption overlap and the consequent FRET are supported by the changing trends of both GRE and RRE as a function of added Sn^{2+} concentration, with UCNP as the energy donor and Sn^{2+} ion-coordinated RBD as the energy acceptor. High R^2 linear fits are obtained for both the GRE (0.9925) and RRE (99 809) forms, demonstrating very precise and reliable Sn^{2+} sensing. In the presence of different Sn^{2+} concentrations (0–50 μM), the ratio of I_{542}/I_{655} and I_{579}/I_{655} varies from 4.9 to 1.0 and 0.01 to 0.24, respectively, exhibiting strong linear correlation ($I_{542}/I_{655} = -0.0776x + 4.7569$, $R^2 = 0.9925$ and $I_{579}/I_{655} = 0.0046x + 0.0175$, $R^2 = 0.9980$, where x is the concentration of Sn^{2+} ions in μM).

The slope of the calibration curves determines the sensitivity of the Sn^{2+} measurement. The GRE and RRE are found to have sensitivities of 0.0776 and 0.0046 per unit change in concentration (in μM), respectively. This ratiometric analysis can be utilized to calculate the Sn^{2+} ion concentration because free RBD coordinated with Sn^{2+} ion does not show any fluorescence under the 980 nm excitation. The RBD emission intensity response to Sn^{2+} ion concentration has a strong linear coefficient (R^2) up to 0.99809, implying excellent quantification capabilities. The detection limit (3σ) by utilizing this FRET-based upconverting nanophosphor photoluminescence spectroscopy is found to be as low as 10 nM (0.01092 μM), which is more than 10-fold better than that observed using

UV–vis and fluorescence techniques for free RBD treated with Sn^{2+} ions. The determined detection limit is far lower than the World Health Organization (WHO) approved Sn^{2+} contamination levels of 2.1×10^{-6} and 8.4×10^{-4} M for drinking water and other products, respectively.⁵⁸ When compared to some other reported probes, the UCNP@PAA-RBD nanoprobe shows a better detection limit for Sn^{2+} ions, as shown in Table 1.

Table 1. Comparison of Detection Limits for Sn^{2+} Ion Using UCNP@PAA-RBD with Other Reported Probes

S. No.	probe name	media	method	detection limit (μM)	reference
1	SEPTD	DMF	absorption/emission	0.17	59
2	2CND	water	emission	0.41	60
3	copolyimides	methanol	quenching	1.9	61
4	carbazole-containing diarylethene	methanol	emission	1.9	62
5	rhodamine-B with <i>tert</i> -butyl carbazate group (R2)	ethanol/water	emission	0.46	63
6	Rh-ED	ethanol/water	emission	0.16	64
7	diamine Schiff base ligand (L)	DMSO/water	absorption/emission	0.31	24
8	CK	PBD/ethanol	emission	0.11	65
9	GO-CeM	HAc-NaAc/TMB	colorimetry	5.58	66
10	UCNP@PAA-RBD	water	FRET	0.01	this work

The ratio of the emission intensity at 579 nm (I_{579}) to the intensity at 542 nm (I_{542}) and *vice versa*, against the Sn^{2+} concentration range from 0 to 50 μM , are shown in Figure S8A,C, respectively, which shows an exponential variation in the ratios. However, the plots of logarithmic emission intensity ratios for the same against the concentration of Sn^{2+} ions were

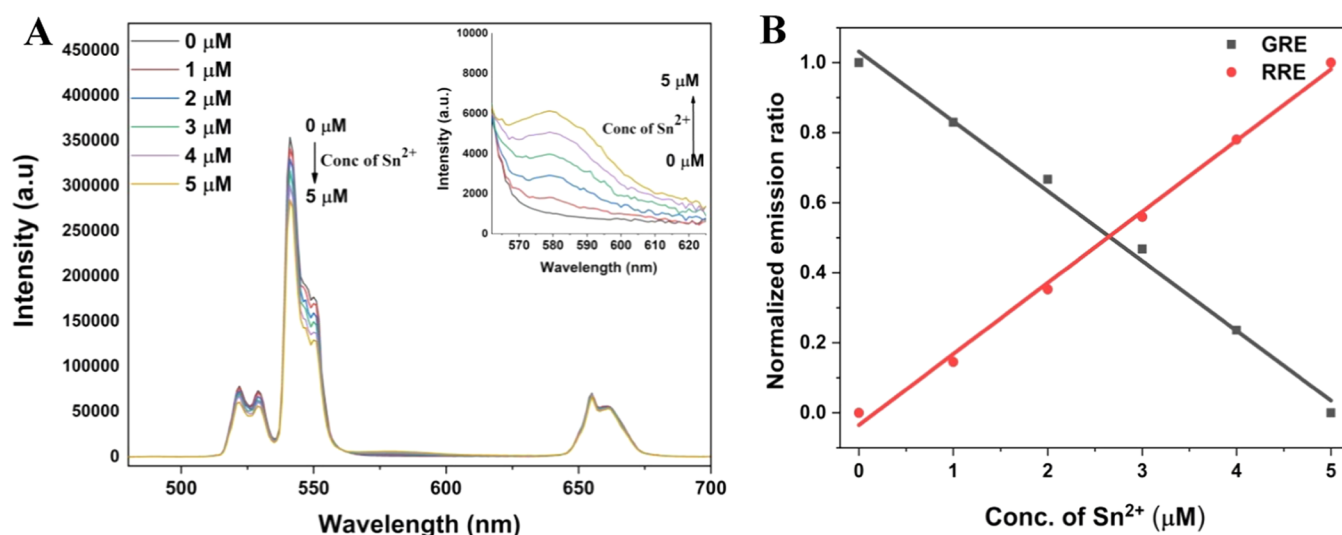


Figure 9. (A) Upconversion emission spectra of UCNP@PAA-RBD upon addition of Sn^{2+} ions below $5 \mu\text{M}$. (B) Variation in normalized GRE and RRE at the Sn^{2+} ion concentration of $0\text{--}5 \mu\text{M}$.

found to have a good linear relationship (Figure S8B,D). In the range of $0\text{--}50 \mu\text{M}$, R^2 is 0.9936, which was the linear correlation coefficient. Figure 9A shows the FRET process using the nanoprobe using an even more subtle variation in the Sn^{2+} ion concentration ($1\text{--}5 \mu\text{M}$). As we observe from the graph, the FRET resulting in the variation of such low analyte concentration is visually noticeable from the spectra; even $1 \mu\text{M}$ of Sn^{2+} ions alter the green emission peak because of the efficient FRET process in the nanoprobe. The normalized GRE and RRE ratio at different concentrations of Sn^{2+} ($0\text{--}5 \mu\text{M}$) is shown in Figure 9B. Here, we also obtain high R^2 linear fits for both GRE and RRE, which is similar to the previous data, again confirming the high sensitivity toward Sn^{2+} ions as shown in Figure S9. The ratios of I_{542}/I_{655} and I_{579}/I_{655} for the concentration ranges from 0 to $5 \mu\text{M}$ exhibit a strong linear correlation ($I_{542}/I_{655} = -0.1514x + 5.0246$, $R^2 = 0.9935$ and $I_{579}/I_{655} = 0.0156x + 0.0121$, $R^2 = 0.9962$, where x is the concentration of Sn^{2+} ions in μM). The detection limit (3σ) from this low-concentration data was observed to be 10 nM ($0.010248 \mu\text{M}$), which correlates with the data taken for the concentration range of $0\text{--}50 \mu\text{M}$ for Sn^{2+} ions. Further, the actual and logarithmic ratios of emission intensity at 579 nm (I_{579}) to intensity at 542 nm (I_{542}) and *vice versa*, against Sn^{2+} concentration ranges from 0 to $5 \mu\text{M}$, are shown in Figure S10, which shows an exponential correlation of the actual ratios and a linear correlation for the logarithmic ratios with analyte concentration. The pH-dependent response of UCNP@PAA-RBD toward Sn^{2+} detection has also been examined. The upconverting emission spectra of UCNP@PAA-RBD, with and without Sn^{2+} ions, in the pH range of $4\text{--}9$ are recorded and the GRE and RRE responses are analyzed. As illustrated in Figure S11A,B, the variation in GRE and RRE before the addition of Sn^{2+} ions is negligible, but in the acidic and alkaline pH, the green emission intensity of UCNP is still less compared to that in neutral pH. After the addition of Sn^{2+} ions ($10 \mu\text{M}$), the efficient energy transfer has been observed from the graph (the GRE values decrease and RRE values increase in all pH values), indicating that pH has little impact on the FRET process and detection analysis. These results further confirm the successful transfer of energy between the UCNP and RBD even at a low analyte concentration and in a wider pH range.

Therefore, these nanophosphor-based probes can be used for the ultrasensitive detection of Sn^{2+} ions in various samples, following NIR excitation.

CONCLUSIONS

In summary, we have developed polymer-modified and RBD-functionalized upconverting nanophosphors for the FRET-based ultrasensitive detection of Sn^{2+} ions. Here, UCNPs acted as the energy donor and convert the NIR (980 nm) into visible light, which was absorbed by the RBD molecules only in the presence of Sn^{2+} ions. This nanoprobe exhibited a fast response to Sn^{2+} ions, a low autofluorescence background, and strong selectivity. With the addition of Sn^{2+} ions, the nanoprobe generated a clear color shift from colorless to magenta, which could be seen with the naked eye, accompanied by an increase in fluorescence emission. More importantly, when excited by NIR (980 nm) light, the intensity of green upconversion emissions reduced progressively, while a new emission peak at 579 nm developed, which grew with increasing Sn^{2+} ion concentration, corresponding to the efficient FRET from UCNP to the RBD- Sn^{2+} complex. The ratiometric approach provided an efficient and reliable response for the detection of Sn^{2+} with a detection limit of $0.01 \mu\text{M}$, which is a tenth of that of pure RBD and is lower than the WHO-approved contamination levels of Sn^{2+} ions. This demonstrates that the nanophosphors have high sensitivity and selectivity toward Sn^{2+} ions and can be used to detect under the excitation of NIR light.

ASSOCIATED CONTENT

Supporting Information

The Supporting Information is available free of charge at <https://pubs.acs.org/doi/10.1021/acsomega.2c02671>.

DLS (S1) and EDX (S2) spectra of UCNP, ^1H NMR and ^{13}C NMR (S3) spectra of the as-synthesized RBD, fluorescence spectra (S4A) for the selectivity and time response of RBD (S4B), calibration plots (S5–S10) for FRET-based sensitivity and pH-dependent behavior of nanoprobe (S11A,B) (PDF)

AUTHOR INFORMATION

Corresponding Author

Indrajit Roy – Department of Chemistry, University of Delhi, Delhi 110007, India; orcid.org/0000-0001-9066-7906; Email: indrajitroy11@gmail.com

Author

Jitender Kumar – Department of Chemistry, University of Delhi, Delhi 110007, India

Complete contact information is available at:

<https://pubs.acs.org/10.1021/acsomega.2c02671>

Notes

The authors declare no competing financial interest.

ACKNOWLEDGMENTS

This work is supported by funding provided by the Institution of Eminence (IoE), University of Delhi, India. J.K. acknowledges senior research fellowship (SRF) support provided by the Council of Scientific and Industrial Research (CSIR), India.

REFERENCES

- (1) Liu, J.; Wu, K.; Li, X.; Han, Y.; Xia, M. A Water Soluble Fluorescent Sensor for the Reversible Detection of Tin(IV) Ion and Phosphate Anion. *RSC Adv.* **2013**, *3*, 8924–8928.
- (2) Ciacci, L.; Reck, B. K.; Nassar, N. T.; Graedel, T. E. Lost by Design. *Environ. Sci. Technol.* **2015**, *49*, 9443–9451.
- (3) Kucklick, J. R.; Ellisor, M. D. A Review of Organotin Contamination in Arctic and Subarctic Regions. *Emerging Contam.* **2019**, *5*, 150–156.
- (4) Hoch, M. Organotin Compounds in the Environment — an Overview. *Appl. Geochem.* **2001**, *16*, 719–743.
- (5) Tuzen, M.; Uluozlu, O. D.; Mendil, D.; Soylak, M.; Machado, L. O. R.; dos Santos, W. N. L.; Ferreira, S. L. C. A Simple, Rapid and Green Ultrasound Assisted and Ionic Liquid Dispersive Microextraction Procedure for the Determination of Tin in Foods Employing ETAAS. *Food Chem.* **2018**, *245*, 380–384.
- (6) Velusamy, S.; Roy, A.; Sundaram, S.; Kumar Mallick, T. A Review on Heavy Metal Ions and Containing Dyes Removal Through Graphene Oxide-Based Adsorption Strategies for Textile Wastewater Treatment. *Chem. Rec.* **2021**, *21*, 1570–1610.
- (7) Malik, L. A.; Bashir, A.; Qureshi, A.; Pandith, A. H. Detection and Removal of Heavy Metal Ions: A Review. *Environ. Chem. Lett.* **2019**, *17*, 1495–1521.
- (8) Fu, Z.; Xi, S. The Effects of Heavy Metals on Human Metabolism. *Toxicol. Mech. Methods* **2019**, *30*, 167–176.
- (9) Tomza-Marciniak, A.; Pilarczyk, B.; Marciniak, A.; Pilarczyk, R.; Bąkowska, M. Tin, Sn. In *Mammals and Birds as Bioindicators of Trace Element Contaminations in Terrestrial Environments*; Springer, 2019; pp 693–708.
- (10) Poddalgoda, D.; Macey, K.; Jayawardene, I.; Krishnan, K. Derivation of Biomonitoring Equivalent for Inorganic Tin for Interpreting Population-Level Urinary Biomonitoring Data. *Regul. Toxicol. Pharmacol.* **2016**, *81*, 430–436.
- (11) Ostrakhovitch, E. A. Tin. In *Handbook on the Toxicology of Metals*; Elsevier, 2022; pp 807–856.
- (12) Du, J.; Zhao, M.; Huang, W.; Deng, Y.; He, Y. Visual Colorimetric Detection of Tin(II) and Nitrite Using a Molybdenum Oxide Nanomaterial-Based Three-Input Logic Gate. *Anal. Bioanal. Chem.* **2018**, *410*, 4519–4526.
- (13) Rahayu, E. F.; Asmorowati, D. S. Review of Metal Corrosion on Food Cans. *J. Phys. Conf. Ser.* **2019**, *1321*, No. 022037.
- (14) Zhang, S.; Li, P.; Li, Z. H. Toxicity of Organotin Compounds and the Ecological Risk of Organic Tin with Co-Existing Contaminants in Aquatic Organisms. *Comp. Biochem. Physiol., Part C: Toxicol. Pharmacol.* **2021**, *246*, No. 109054.
- (15) Granjeiro, J. M.; Cruz, R.; Leite, P. E.; Gemini-Piperni, S.; Boldrini, L. C.; Ribeiro, A. R. Health and Environment Perspective of Tin Nanocompounds: A Safety Approach. *Tin Oxide Mater.* **2020**, *133*–162.
- (16) Saha, S.; Kamila, S.; Chattopadhyay, A.; Sahoo, P. Easy and Rapid Chemosensing Method for the Identification of Accumulated Tin in Algae: A Strategy to Protect a Marine Eco-System. *New J. Chem.* **2022**, *46*, 4233–4238.
- (17) Ni, X.; Cheng, H. S. Seizure Failure of Copper-Lead with Overlay and Aluminum-Tin Connecting Rod Bearings. *Tribol. Trans.* **2008**, *39*, 194–200.
- (18) Györi, J.; Platoshyn, O.; Carpenter, D. O.; Salánki, J. Effect of Inorganic and Organic Tin Compounds on ACh- and Voltage-Activated Na Currents. *Cell. Mol. Neurobiol.* **2000**, *20*, 591–604.
- (19) Aiyegbusi, O.; McGregor, L.; McGeoch, L.; Kipgen, D.; Geddes, C. C.; Stevens, K. I. Renal Disease in Primary Sjögren's Syndrome. *Rheumatol. Ther.* **2021**, *8*, 63–80.
- (20) Zachariadis, G. A.; Rosenberg, E. Speciation Analysis of Triethyl-Lead and Tributyl-Tin Compounds in Human Urine by Liquid–Liquid Extraction and Gas Chromatography Microwave-Induced Plasma Atomic Emission Detection. *J. Sep. Sci.* **2012**, *35*, 1132–1137.
- (21) Tutschku, S.; Schantz, M. M.; Wise, S. A. Determination of Methylmercury and Butyltin Compounds in Marine Biota and Sediments Using Microwave-Assisted Acid Extraction, Solid-Phase Microextraction, and Gas Chromatography with Microwave-Induced Plasma Atomic Emission Spectrometric Detection. *Anal. Chem.* **2002**, *74*, 4694–4701.
- (22) Gras, R.; Luong, J.; Shellie, R. A. Direct Measurement of Elemental Mercury Using Multidimensional Gas Chromatography with Microwave-Induced Helium Plasma Atomic Emission Spectroscopy. *ACS Earth Space Chem.* **2018**, *2*, 471–478.
- (23) Zachariadis, G. A.; Rosenberg, E. Determination of Butyl- and Phenyltin Compounds in Human Urine by HS-SPME after Derivatization with Tetraethylborate and Subsequent Determination by Capillary GC with Microwave-Induced Plasma Atomic Emission and Mass Spectrometric Detection. *Talanta* **2009**, *78*, 570–576.
- (24) Kolcu, F.; Erdener, D.; Kaya, İ. Synthesis and Characterization of a Highly Selective Turn-on Fluorescent Chemosensor for Sn²⁺ Derived from Diimine Schiff Base. *Synth. Met.* **2021**, *272*, No. 116668.
- (25) Niu, Y.; Li, J.; Gao, J.; Ouyang, X.; Cai, L.; Xu, Q. Two-Dimensional Quantum Dots for Biological Applications. *Nano Res.* **2021**, *14*, 3820–3839.
- (26) Xu, Q.; Niu, Y.; Li, J.; Yang, Z.; Gao, J.; Ding, L.; Ni, H.; Zhu, P.; Liu, Y.; Tang, Y.; Lv, Z.-P.; Peng, B.; Hu, T. S.; Zhou, H.; Xu, C. Recent Progress of Quantum Dots for Energy Storage Applications. *Carbon Neutrality* **2022**, *1*, 1–18.
- (27) Wang, Y.; Bian, Y.; Chen, X.; Su, D. Chemiluminescent Probes Based on 1,2-Dioxetane Structures For Bioimaging. *Chem. - Asian J.* **2022**, *17*, No. e202200018.
- (28) del Rosal, B.; del Benayas, A. Strategies to Overcome Autofluorescence in Nanoprobe-Driven In Vivo Fluorescence Imaging. *Small Methods* **2018**, *2*, No. 1800075.
- (29) Finlayson, L.; Barnard, I. R. M.; McMillan, L.; Ibbotson, S. H.; Brown, C. T. A.; Eadie, E.; Wood, K. Depth Penetration of Light into Skin as a Function of Wavelength from 200 to 1000 Nm. *Photochem. Photobiol.* **2022**, *98*, 974–981.
- (30) Cai, Y.; Wei, Z.; Song, C.; Tang, C.; Han, W.; Dong, X. Optical Nano-Agents in the Second near-Infrared Window for Biomedical Applications. *Chem. Soc. Rev.* **2019**, *48*, 22–37.
- (31) Wu, J. L.; Chen, F. C.; Chuang, M. K.; Tan, K. S. Near-Infrared Laser-Driven Polymer Photovoltaic Devices and Their Biomedical Applications. *Energy Environ. Sci.* **2011**, *4*, 3374–3378.
- (32) Yang, F.; Zhang, Q.; Huang, S.; Ma, D. Recent Advances of near Infrared Inorganic Fluorescent Probes for Biomedical Applications. *J. Mater. Chem. B* **2020**, *8*, 7856–7879.

- (33) Zhang, P.; Wang, H.; Hong, Y.; Yu, M.; Zeng, R.; Long, Y.; Chen, J. Selective Visualization of Endogenous Hypochlorous Acid in Zebrafish during Lipopolysaccharide-Induced Acute Liver Injury Using a Polymer Micelles-Based Ratiometric Fluorescent Probe. *Biosens. Bioelectron.* **2018**, *99*, 318–324.
- (34) Liu, H.; Zhang, P.; Zhang, C.; Chen, J.; Jiang, J. H. Self-Assembly of a Dual-Targeting and Self-Calibrating Ratiometric Polymer Nanoprobe for Accurate Hypochlorous Acid Imaging. *ACS Appl. Mater. Interfaces* **2020**, *12*, 45822–45829.
- (35) Zhang, P.; Nie, X.; Gao, M.; Zeng, F.; Qin, A.; Wu, S.; Tang, B. Z. A Highly Selective Fluorescent Nanoprobe Based on AIE and ES IPT for Imaging Hydrogen Sulfide in Live Cells and Zebrafish. *Mater. Chem. Front.* **2017**, *1*, 838–845.
- (36) Sun, L.; Wei, R.; Feng, J.; Zhang, H. Tailored Lanthanide-Doped Upconversion Nanoparticles and Their Promising Bioapplication Prospects. *Coord. Chem. Rev.* **2018**, *364*, 10–32.
- (37) Wang, J.; Sheng, T.; Zhu, X.; Li, Q.; Wu, Y.; Zhang, J.; Liu, J.; Zhang, Y. Spectral Engineering of Lanthanide-Doped Upconversion Nanoparticles and Their Biosensing Applications. *Mater. Chem. Front.* **2021**, *5*, 1743–1770.
- (38) Idris, N. M.; Jayakumar, M. K. G.; Bansal, A.; Zhang, Y. Upconversion Nanoparticles as Versatile Light Nanotransducers for Photoactivation Applications. *Chem. Soc. Rev.* **2015**, *44*, 1449–1478.
- (39) Jee, H.; Chen, G.; Prasad, P. N.; Ohulchanskyy, T. Y.; Lee, J. In Situ Ultraviolet Polymerization Using Upconversion Nanoparticles: Nanocomposite Structures Patterned by Near Infrared Light. *Nanomaterials* **2020**, *10*, 2054.
- (40) Wen, S.; Zhou, J.; Schuck, P. J.; Suh, Y. D.; Schmidt, T. W.; Jin, D. Future and Challenges for Hybrid Upconversion Nanosystems. *Nat. Photonics* **2019**, *13*, 828–838.
- (41) Kumar, B.; Malhotra, K.; Fuku, R.; Van Houten, J.; Qu, G. Y.; Piuanno, P. A. E.; Krull, U. J. Recent Trends in the Developments of Analytical Probes Based on Lanthanide-Doped Upconversion Nanoparticles. *TrAC Trends Anal. Chem.* **2021**, *139*, No. 116256.
- (42) Chen, B.; Wang, F. Recent Advances in the Synthesis and Application of Yb-Based Fluoride Upconversion Nanoparticles. *Inorg. Chem. Front.* **2020**, *7*, 1067–1081.
- (43) Wen, S.; Zhou, J.; Zheng, K.; Bednarkiewicz, A.; Liu, X.; Jin, D. Advances in Highly Doped Upconversion Nanoparticles. *Nat. Commun.* **2018**, *9*, No. 2415.
- (44) Shang, X.; Chen, P.; Jia, T.; Feng, D.; Zhang, S.; Sun, Z.; Qiu, J. Upconversion Luminescence Mechanisms of Er³⁺ Ions under Excitation of an 800 Nm Laser. *Phys. Chem. Chem. Phys.* **2015**, *17*, 11481–11489.
- (45) Duan, C.; Liang, L.; Li, L.; Zhang, R.; Xu, Z. P. Recent Progress in Upconversion Luminescence Nanomaterials for Biomedical Applications. *J. Mater. Chem. B* **2018**, *6*, 192–209.
- (46) Wang, Y.; Zheng, K.; Song, S.; Fan, D.; Zhang, H.; Liu, X. Remote Manipulation of Upconversion Luminescence. *Chem. Soc. Rev.* **2018**, *47*, 6473–6485.
- (47) Lingeshwar Reddy, K.; Balaji, R.; Kumar, A.; Krishnan, V. Lanthanide Doped Near Infrared Active Upconversion Nanophosphors: Fundamental Concepts, Synthesis Strategies, and Technological Applications. *Small* **2018**, *14*, No. 1801304.
- (48) Liu, Y.; Ouyang, Q.; Li, H.; Chen, M.; Zhang, Z.; Chen, Q. Turn-On Fluorescence Sensor for Hg²⁺ in Food Based on FRET between Aptamers-Functionalized Upconversion Nanoparticles and Gold Nanoparticles. *J. Agric. Food Chem.* **2018**, *66*, 6188–6195.
- (49) Ding, Y.; Zhu, H.; Zhang, X.; Zhu, J. J.; Burda, C. Rhodamine B Derivative-Functionalized Upconversion Nanoparticles for FRET-Based Fe³⁺-Sensing. *Chem. Commun.* **2013**, *49*, 7797–7799.
- (50) Ansari, A. A.; Thakur, V. K.; Chen, G. Functionalized Upconversion Nanoparticles: New Strategy towards FRET-Based Luminescence Bio-Sensing. *Coord. Chem. Rev.* **2021**, *436*, No. 213821.
- (51) Chi, D.; Cui, S.; Chen, H.; Gu, Y. Comparison of Two Strategies for the Synthesis of Upconverting Nanoparticles as Biological Labels. *J. Phys. Conf. Ser.* **2011**, *277*, No. 012006.
- (52) Kong, W.; Sun, T.; Chen, B.; Chen, X.; Ai, F.; Zhu, X.; Li, M.; Zhang, W.; Zhu, G.; Wang, F. A General Strategy for Ligand Exchange on Upconversion Nanoparticles. *Inorg. Chem.* **2017**, *56*, 872–877.
- (53) Park, Y. I.; Nam, S. H.; Kim, J. H.; Bae, Y. M.; Yoo, B.; Kim, H. M.; Jeon, K. S.; Park, H. S.; Choi, J. S.; Lee, K. T.; Suh, Y. D.; Hyeon, T. Comparative Study of Upconverting Nanoparticles with Various Crystal Structures, Core/Shell Structures, and Surface Characteristics. *J. Phys. Chem. C* **2013**, *117*, 2239–2244.
- (54) Radunz, S.; Schavkan, A.; Wahl, S.; Würth, C.; Tschiche, H. R.; Krumrey, M.; Resch-Genger, U. Evolution of Size and Optical Properties of Upconverting Nanoparticles during High-Temperature Synthesis. *J. Phys. Chem. C* **2018**, *122*, 28958–28967.
- (55) Yao, L.; Li, Y.; Xu, D.; Lin, H.; Peng, Y.; Yang, S.; Zhang, Y. Simultaneous Enhancement of Upconversion Luminescence and Thermometric Property of Upconversion Nanoparticles by Tuning Crystal Field. *J. Lumin.* **2019**, *211*, 144–149.
- (56) Liao, J.; Jin, D.; Chen, C.; Li, Y.; Zhou, J. Helix Shape Power-Dependent Properties of Single Upconversion Nanoparticles. *J. Phys. Chem. Lett.* **2020**, *11*, 2883–2890.
- (57) Han, J.; Zhang, C.; Liu, F.; Liu, B.; Han, M.; Zou, W.; Yang, L.; Zhang, Z. Upconversion Nanoparticles for Ratiometric Fluorescence Detection of Nitrite. *Analyst* **2014**, *139*, 3032–3038.
- (58) Wang, J.; Lv, M.; Wang, Z.; Zhou, M.; Gu, C.; Guo, C. Highly Sensitive and Selective Fluorescent Detection of Rare Earth Metal Sn(II) Ion by Organic Fluorine Schiff Base Functionalized Periodic Mesoporous Material in Aqueous Solution. *J. Photochem. Photobiol., A* **2015**, *309*, 37–46.
- (59) Ye, X. L.; Li, P.; Liu, Y. L.; Liang, X. M.; Yang, L. A Dual-Mode Fluorescent Probe Based on Perylene for the Detection of Sn²⁺. *Inorg. Chem. Commun.* **2021**, *130*, No. 108739.
- (60) Ravichandiran, P.; Prabakaran, D. S.; Bella, A. P.; Boguszewska-Czubara, A.; Maslyk, M.; Dineshkumar, K.; Johnson, P. M.; Park, B. H.; Han, M. K.; Kim, H. G.; Yoo, D. J. Naphthoquinone-Dopamine Linked Colorimetric and Fluorescence Chemosensor for Selective Detection of Sn²⁺ Ion in Aqueous Medium and Its Bio-Imaging Applications. *ACS Sustainable Chem. Eng.* **2020**, *8*, 10947–10958.
- (61) Thelakkat, M.; Pösch, P.; Schmidt, H. W. Synthesis and Characterization of Highly Fluorescent Main-Chain Copolyimides Containing Perylene and Quinoxaline Units. *Macromolecules* **2001**, *34*, 7441–7447.
- (62) Qu, S.; Zheng, C.; Liao, G.; Fan, C.; Liu, G.; Pu, S. A Fluorescent Chemosensor for Sn²⁺ and Cu²⁺ Based on a Carbazole-Containing Diarylethene. *RSC Adv.* **2017**, *7*, 9833–9839.
- (63) Lan, H.; Wen, Y.; Shi, Y.; Liu, K.; Mao, Y.; Yi, T. Fluorescence Turn-on Detection of Sn²⁺ in Live Eukaryotic and Prokaryotic Cells. *Analyst* **2014**, *139*, 5223–5229.
- (64) Rathinam, B.; Murugesan, V.; Liu, B.-T. Fluorescent “OFF–ON” Sensors for the Detection of Sn²⁺ Ions Based on Amine-Functionalized Rhodamine 6G. *Chemosensors* **2022**, *10*, 69.
- (65) Kong, Y.; Wang, M.; Lu, W.; Li, L.; Li, J.; Chen, M.; Wang, Q.; Qin, G.; Cao, D. Rhodamine-Based Chemosensor for Sn²⁺ Detection and Its Application in Nanofibrous Film and Bioimaging. *Anal. Bioanal. Chem.* **2022**, *414*, 2009–2019.
- (66) Singh, G.; Kushwaha, A.; Sharma, M. Persistent Peroxidase Mimics of Graphene Oxide Anchored Cerium Molybdate Sensor: An Effective Colorimetric Detection of S²⁻ and Sn²⁺ Ions. *Microchem. J.* **2020**, *153*, No. 104290.